Color-Selective Printed Organic Photodiodes for Filterless Multichannel Visible Light Communication

Noah Strobel, Nikolaos Droseros, Wolfgang Köntges, Mervin Seiberlich, Manuel Pietsch, Stefan Schlisske, Felix Lindheimer, Rasmus R. Schröder, Uli Lemmer, Martin Pfannmöller, Natalie Banerji, and Gerardo Hernandez-Sosa*

Future lightweight, flexible, and wearable electronics will employ visible-light-communication schemes to interact within indoor environments. Organic photodiodes are particularly well suited for such technologies as they enable chemically tailored optoelectronic performance and fabrication by printing techniques on thin and flexible substrates. However, previous methods have failed to address versatile functionality regarding wavelength selectivity without increasing fabrication complexity. This work introduces a general solution for printing wavelength-selective bulk-heterojunction photodetectors through engineering of the ink formulation. Nonfullerene acceptors are incorporated in a transparent polymer donor matrix to narrow and tune the response in the visible range without optical filters or light-management techniques. This approach effectively decouples the optical response from the viscoelastic ink properties, simplifying process development. A thorough morphological and spectroscopic investigation finds excellent charge-carrier dynamics enabling state-of-the-art responsivities $>10^2$ mA W^{-1} and cutoff frequencies >1.5 MHz. Finally, the color selectivity and high performance are demonstrated in a filterless visible-light-communication system capable of demultiplexing intermixed optical signals.

Light detection represents one of the fundamental pillars of modern technology as it enables a variety of everyday applications in optical communications, medical diagnostics and imaging systems.[1,2] In order to match the required benchmarks of these technologies, the detector characteristics need to be tailored to the final application in terms of optoelectronic performance and device design. This is particularly relevant to upcoming technologies such as visible light communication (VLC) which aims to provide indoor navigation in buildings, direct and secure optical data links as well as high-speed communication by using ambient lighting to transmit data.[3,4] In the scope of multichannel communication, high requirements in terms of spectral selectivity should be met in addition to a fabrication route compatible with future mobile and wearable devices based on lightweight and flexible electronics. Organic photodiodes (OPDs) are particularly well suited for this purpose since the synthetic flexibility of the materials can be exploited to tailor a specific device figure of merit such as their spectral selectivity.[5–10] Very recently, this energetic tunability allowed record efficiencies of 26% for indoor light harvesting to be reached.[11] Additionally, their processability via printing techniques enables high-throughput additive manufacturing on thin and mechanically flexible substrates with full freedom of design.[12–15] Previous studies have shown that printed OPDs can compete with commercial photodiodes based on inorganic materials in terms of responsivity, dark current and linear dynamic range.[16–21] However, in their great majority, these OPDs utilize active layers developed for

---

N. Strobel, M. Seiberlich, M. Pietsch, S. Schlisske, F. Lindheimer, Prof. U. Lemmer, Dr. G. Hernandez-Sosa
Light Technology Institute
Karlsruhe Institute of Technology
Engesserstrasse 13, 76131 Karlsruhe, Germany
E-mail: gerardo.sosa@kit.edu
N. Strobel, M. Seiberlich, M. Pietsch, S. Schlisske, F. Lindheimer, Dr. G. Hernandez-Sosa
InnovationLab
Speyerer Strasse 4, 69115 Heidelberg, Germany

N. Droseros, Prof. N. Banerji
Department of Chemistry and Biochemistry
University of Bern
Freiestrasse 3, CH-3012 Bern, Switzerland
W. Köntges, Prof. R. R. Schröder, Dr. M. Pfannmöller
Centre for Advanced Materials
Heidelberg University
Im Neuenheimer Feld 225, 69120 Heidelberg, Germany
Prof. U. Lemmer
Institute of Microstructure Technology
Karlsruhe Institute of Technology
Hermann-von-Helmholtz-Platz 1, 76344 Eggenstein-Leopoldshafen
Germany

ADVANCED
SCIENCE NEWS
www.advancedsciencenews.com

ADVANCED
MATERIALS
www.advmat.de

photovoltaic applications and are therefore designed to have a broad absorption range which aims to match the solar spectrum.[14] As such, these devices have relied on device engineering approaches to limit their spectral responsivity range. Recently, solution-processed wavelength selective OPDs have been realized by means of: i) optical filtering,[5,22] ii) charge collection narrowing,[23–25] and iii) cavity enhanced absorption.[26–28] All of these techniques have demonstrated wavelength selective responsivity and enabled successful application in color reconstruction or IR-spectroscopy. However, all three approaches present challenges that limit their technological transfer toward industrially relevant printing techniques. These challenges include: i) additional layers and processing steps, ii) time investment in ink formulation for different active layers, and iii) high optical quality demands regarding layer homogeneity and thickness.

Here we present a filterless concept for inkjet-printed color-selective OPDs which exploits the selective absorption of a bulk-heterojunction (BHJ) system comprised of a transparent wide-bandgap polymer donor and nonfullerene acceptors (NFAs). In this approach, the device spectral response solely depends on the choice of the NFA while the polymer donor dictates the rheological properties of the ink. This removes any interdependence between processing parameters and the optical properties of the active layer thereby eliminating the need for new ink formulations when selecting a different NFA. Using transient absorption (TA) measurements and analytical transmission electron microscopy (ATEM), we show that these novel BHJs fulfill the required prerequisites from an energetic and morphological perspective and therefore show efficient exciton separation and charge extraction. The printed OPDs exhibit complementary responsivities >10^2 mA W^{-1} in the blue/green and red visible spectral range without the need for additional optical filtering. This state-of-the-art response combined with high bandwidths in the MHz range allows effective application in a VLC system. In this system, the color selectivity of the devices enables successful de-multiplexing of optical signals simultaneously transmitted at different wavelengths without any additional optical filters.

Figure 1a shows the absorbance spectra as well as chemical structures of the chosen active layer materials, i.e., the pristine polyindenoflurorene-8-triarylamine (PIF) and its (1:1) blends with the NFAs IDFBR and ITIC-4F. It can be observed that the contribution of PIF to the layer absorption is limited to the UV range of the spectrum, while the absorption range in the visible region is defined solely by the NFA. As observed in Figure 1b, this absorption governs the spectral responsivity of the OPDs under operation and thus, the extent of their color selectivity. At a bias voltage of −8 V, the spectral responsivity of the PIF:IDFBR devices reaches 72 mA W^{-1} and ranges from 450 to 600 nm. The device containing ITIC-4F achieves 229 mA W^{-1} and mainly absorbs above 600 up to 800 nm, reaching the NIR wavelength window. The respective responsivities are comparable or even outmatch previously demonstrated color-selective photodiodes based on organic or perovskite active layers demonstrating the potential of these nonconventional BHJ systems (see Table S1 in the Supporting Information).[6] A photograph of the inkjet-printed multicolor array with "red" and "blue" OPDs is shown in the inset of Figure 1b. The blue and red

colors of the devices originate from the respective red and blue light absorption of PIF:ITIC-4F and PIF:IDFBR.

Figure 1c depicts the viscosity of the pristine PIF ink formulation to which the NFAs were added at a 1:1 ratio. It can be observed that upon addition of the NFAs, the viscosity of the solution is minimally altered within less than ±5% of the PIF value whereas the color change in the solutions is clearly visible. This feature allowed a simplified process development where the printing parameters are developed only for the pristine PIF ink and transferred without additional adjustment to the color-selective inks (see Figure S1 in the Supporting Information). This effective decoupling of the optical characteristics from the ink properties enables considerable reduction of processing complexity and enhanced spectral versatility as the ink-formulation only needs to be carried out once for various color-selective OPDs. Furthermore, the presented approach can be transferred to other transparent polymer donors and NFA combinations as shown in Figure S2 (Supporting Information).

Generally, the functionality of BHJ systems does not only rely on strong and selective absorption of the active layer but also on an efficient exciton separation and charge extraction at the electrodes. Both are assisted by a favorable intermixed morphology.[29] We assume that the energetic alignment requires a HOMO energy offset (ΔE_{HOMO}) between the PIF and the used NFAs to facilitate successful exciton separation and hole injection from the NFAs to PIF. The energy levels of the three materials are schematically displayed in **Figure 2**a. Previous studies report HOMO levels of 5.5, 5.7, and 5.8 eV for PIF,[30] ITIC-4F,[31] and IDFBR,[32] respectively, which would result in ΔE_{HOMO} of 0.2 eV for PIF:ITIC-4F and 0.3 eV for PIF:IDFBR.

The morphology of the respective systems was investigated by ATEM which was successfully used in the past to visualize the material distribution of fullerene[33,34] and nonfullerene[35] based BHJ blends for organic photovoltaics. ATEM uses the difference in optical excitations of the respective materials in the blend. These differences are measured by electron-energy-loss spectroscopy of transmitted electrons through enriched or mixed phases. It allows variations in the local materials phase distribution of the active layer to be spatially resolved with nanoscale resolution.[33] The electron-energy-loss spectra for the pristine PIF, ITIC-4F and IDFBR as well as evaluation details are provided Figure S3 in the Supporting Information. The material distribution maps were obtained by a machine learning approach on a series of energy-filtered images showing variations in optical excitations.[33,36] Figure 2b,c shows the resulting maps, denoting pristine and intermixed phases for the PIF:ITIC-4F and PIF:IDFBR systems, respectively. A clear difference is visible between the two blends demonstrating a significantly larger intimate intermixing of the PIF:ITIC-4F blend compared to that of the PIF:IDFBR layer. Visible domain sizes in the range of 10–20 nm for ITIC-4F are expected to be sufficiently small for exciton diffusion to polymer molecules. On the other hand, due to the larger domains of the PIF:IDFBR blend in the range of 30–50 nm one would expect less efficient charge separation and therefore the slightly lower spectral responsivity compared to PIF:ITIC-4F. However, steady state photoluminescence measurements of the blends show a quenching efficiency above 92% for both NFAs upon addition of the PIF (see Figure S4 in the Supporting Information)
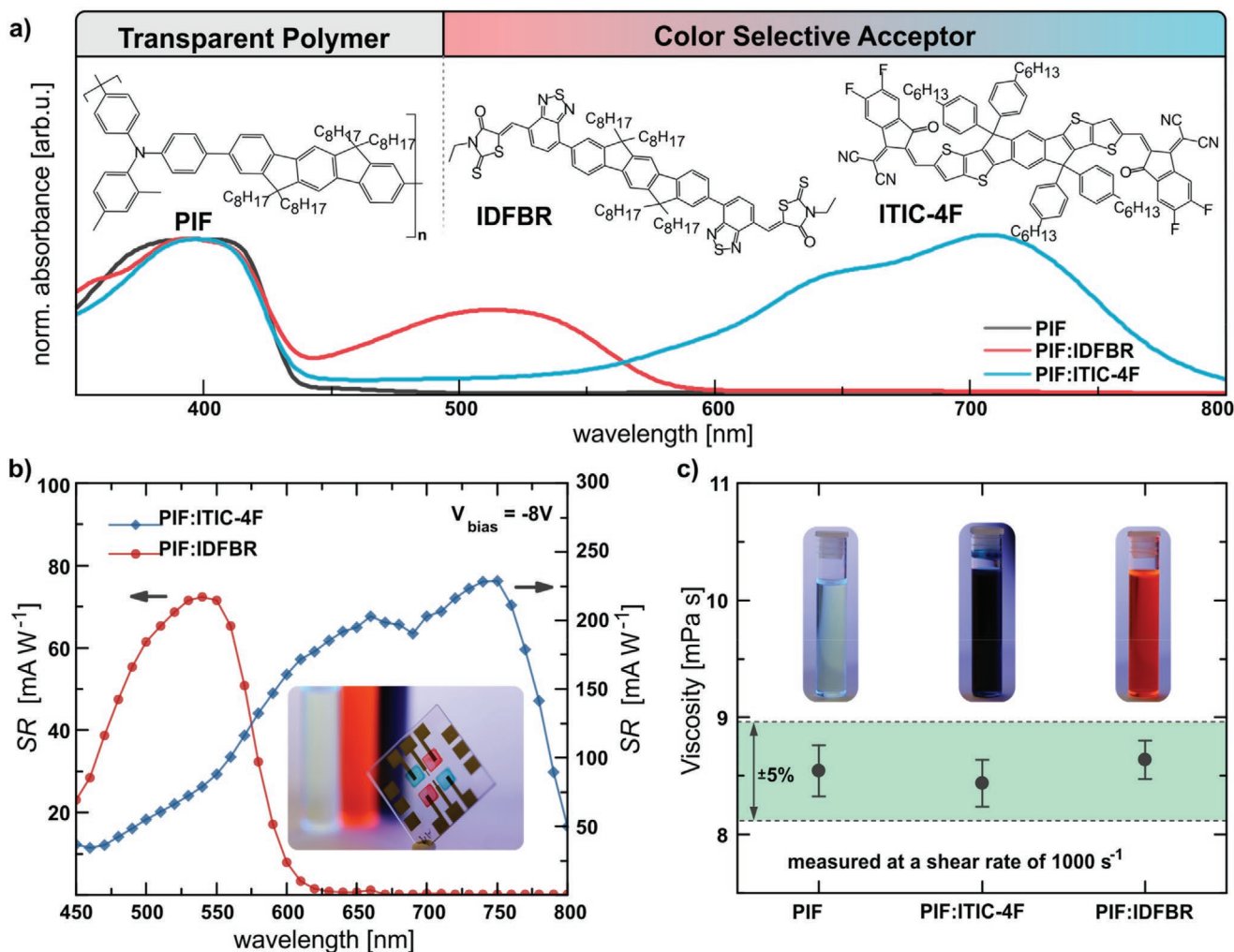
Figure 1. a) Absorbance spectra of the presented material systems comprised of a transparent polymer donor and different NFAs. The latter controls the absorption properties of the blend. The chemical structures of the various materials are shown. b) Spectral responsivity of inkjet-printed devices with the NFAs IDFBR and ITIC-4F realizing green/blue and red selective OPDs, respectively. The inset shows a photograph of the digitally printed dual color array. The device area is 1 mm². c) The viscosities of the different ink formulations used in this work. The inks are based on a 20 g L^{-1} solution of PIF in chlorobenzene. For the blends, NFAs are added at a mass ratio of 1:1.

confirming an efficient separation of the excitons generated in the NFAs. In order to investigate the underlying electronic processes including exciton diffusion, exciton separation and charge injection we studied the two blends by TA. Figure 2d,e shows the TA spectra of the two blends obtained at different time delays after excitation of the acceptor (650 nm for ITIC-4F and 500 nm for IDFBR). The TA spectra of the corresponding neat NFA films at 1 ps are shown for comparison as a black line. For ITIC-4F, it consists of a weak photoinduced absorption (PIA) band below 570 nm, of the acceptor ground-state bleaching (GSB) in the 570–720 nm region, and of the stimulated emission overlapping with the GSB above 700 nm. For IDFBR, the acceptor GSB is seen as a clear negative band below 590 nm, followed by a broad stimulated emission band (590–720 nm) and some PIA above 720 nm. At the earliest time delay of 0.2 ps, the TA spectra of the two blends have a comparable shape as the ones of the photoexcited neat acceptors, confirming selective excitation of the NFA. The GSB as well as

the stimulated emission are blue shifted for both blends compared to the neat NFA films, which is likely due to a different molecular packing and electronic environment. Moreover, we observe a gradual quenching of the stimulated emission signals in the blends, which is accompanied by an increase of the PIA signal in the range of 470–570 nm for PIF:ITIC-4F and 600–740 nm for PIF:IDFBR (insets of Figure 2d,e). The quenching of the stimulated emission and rise of the PIA bands due to photogenerated charges are representative of efficient hole transfer from both excited NFAs to the PIF donor.

In both blends, the spectral changes due to the hole transfer process start immediately after photoexcitation and extend to about 10–20 ps for PIF:ITIC-4F and to about 5–10 ps for PIF:IDFBR, showing that the hole transfer occurs over a broad range of time scales. Using multiexponential global analysis[37] (see details in Figures S6 and S7 in the Supporting Information), we find time constants of 0.3 and 9 ps for the hole transfer in PIF:ITIC-4F, compared to 0.5 and 3.8 ps in
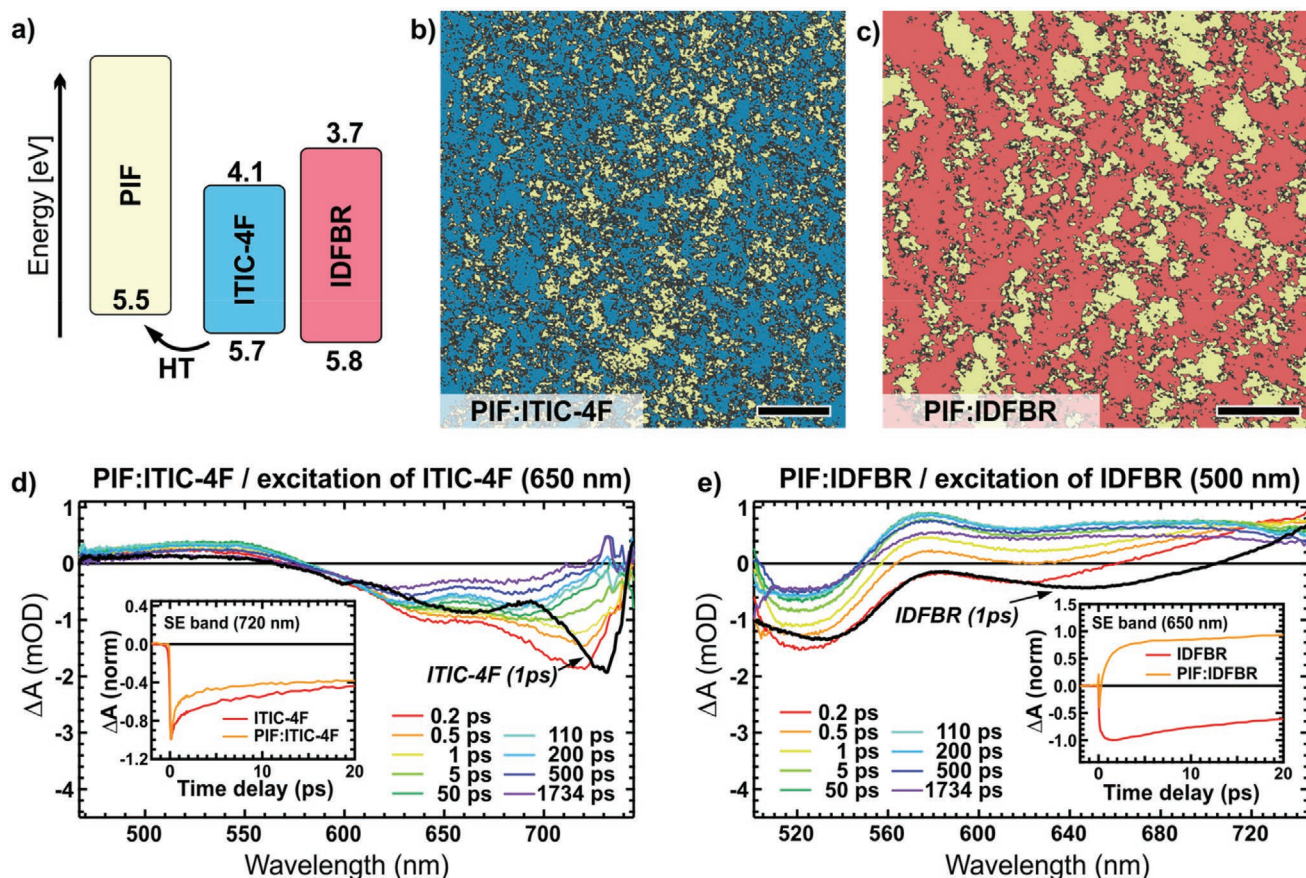
Figure 2. a) Schematic of the energy levels of the materials system. The exciton generated in the NFA splits at the interface between polymer and NFA molecules and the hole is injected to the HOMO of PIF. b,c) Material distribution maps obtained from ATEM spectral analysis of PIF:ITIC-4F (b) and PIF:IDFBR (c). Blue and red represent ITIC-4F and IDFBR domains, respectively. PIF domains are the yellow areas and the interfacial phases are dark gray in both images. Scale bars represent 100 nm. d,e) TA spectra recorded at different time delays after excitation of the acceptor, for PIF:ITIC-4F (d) and PIF:IDFBR (e) blends, with 650 and 500 nm excitation, respectively. The TA spectra of the pristine NFAs with excitation at the same wavelengths are shown as a black line for comparison. The insets show the stimulated emission dynamics of each blend compared to ones of the respective pristine NFAs.

PIF:IDFBR, confirming the slightly faster hole transfer rate in the latter blend. In general, both ultrafast (<1 ps)[38–40] and slower hole transfer (<100 ps) times[41–44] have been shown for high-performance NFA-based systems. The ultrafast component is typically related to the intrinsic hole transfer rate, which is impacted by molecular parameters such as the driving force for charge transfer, while the overall (slower) hole transfer rate can be multiphasic and limited by exciton diffusion over various distances in the complex morphology of the blends. Since the driving forces for hole transfer are comparable in the two blends investigated here (Figure 2a), the intrinsic hole transfer rates take place at the same time scale. Regarding the diffusion-mediated hole transfer, the slightly faster dynamics and larger donor–acceptor domains (Figure 2b,c) of the PIF:IDFBR blend suggest a higher exciton diffusion coefficient compared to that of PIF:ITIC-4F. The dynamics of geminate recombination losses were extracted from the GSB and PIA signatures at long time delays. Both characteristics show a slightly more pronounced decay in the PIF:ITIC-4F blend independent of the excitation wavelength (Figure S7, Supporting Information). This is confirmed from the global analysis, which shows a faster recombination in PIF:ITIC-4F (430 ps) than in PIF:IDFBR

(1.2 ns). The reduced recombination rates, in combination with the suggested higher exciton diffusion coefficient explain the successful exciton separation and charge extraction for the PIF:IDFBR system regardless of the larger phases compared to PIF:ITIC-4F. For completeness, the dynamics of the electron transfer from PIF to the NFAs are also investigated and presented in Figure S5 (Supporting Information). Electron transfer components of 0.2 and 0.8 ps in PIF:ITIC-4F and of 0.2 ps in PIF:IDFBR are observed. Such ultrafast electron transfer is expected for efficient BHJ blends, especially considering the high driving forces as are present here (>1 eV; Figure 2a).[45]

The energetic and morphological characteristics imply that both material systems comply with the requirements of an efficient BHJ. **Figure 3**a–c displays the resulting steady state figures of merit of OPDs comprised of inkjet-printed PIF:NFA active layer on an inkjet-printed electron extraction ZnO layer complemented by an evaporated MO_3 hole extraction layer and Ag electrode. In the dark, both ITIC-4F and IDFBR-based devices show rectifying current–voltage curves, characteristic for diode behavior (Figure 3a). Dark currents below 10 nA cm^{-2} are observed for a bias voltage of −1 V and only increasing to ≈200 nA cm^{-2} at −5 V, demonstrating successful charge

ADVANCED
SCIENCE NEWS
www.advancedsciencenews.com

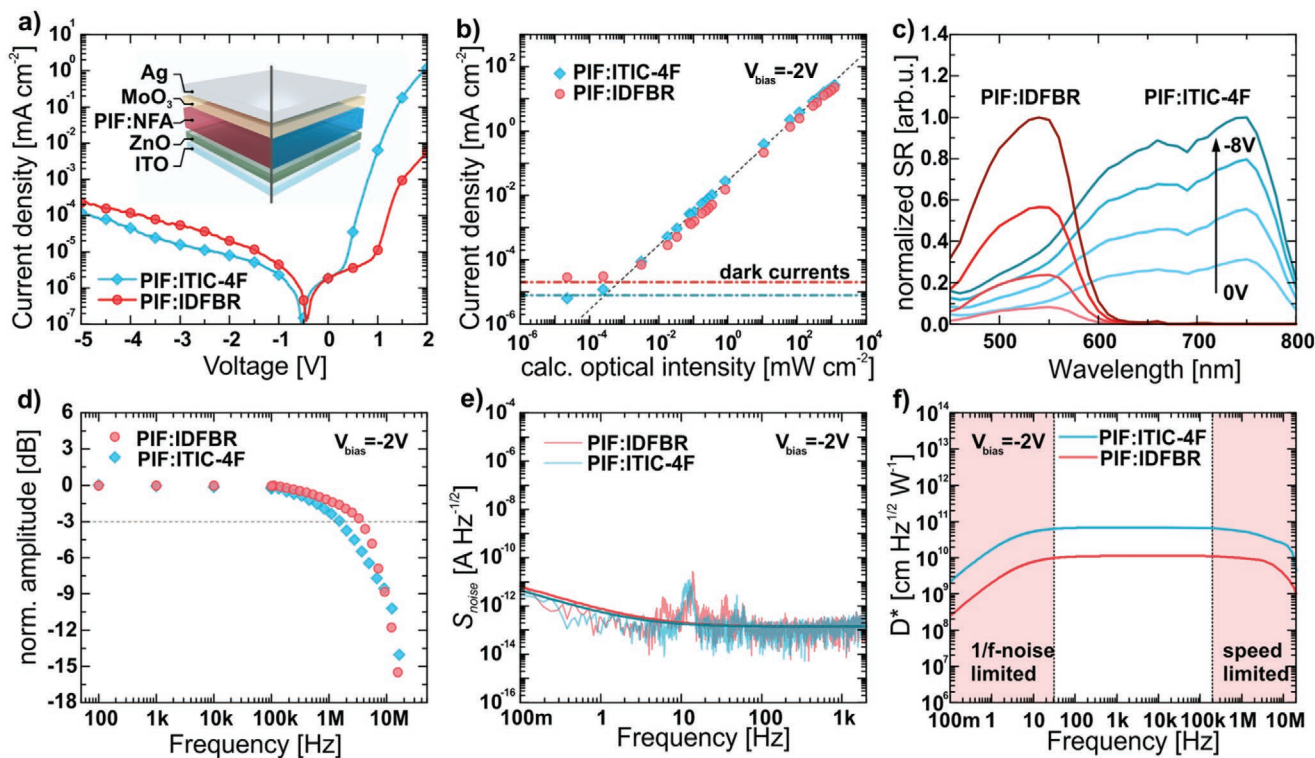ADVANCED
MATERIALS
www.advmat.de

Figure 3. a) Current–voltage characteristics of the printed OPDs in the dark. The inset shows the corresponding devices stack. b) Current response of the devices to different light intensities at −2 V reverse bias. The dotted line represents a slope of unity. c) Responsivity spectra of the two devices for different reverse bias voltages normalized to the corresponding signal at −8 V. d) Cutoff frequency measurement, e) noise spectral density, and f) resulting frequency-dependent specific detectivity of the two printed color-selective OPDs at a reverse bias of −2 V.

blocking of the device stack and high layer quality preventing hot spots prone to breakdown. The lower forward current for the IDFBR device suggests a lower charge injection from the ITO/ZnO electrode to the NFA, which is presumably related to the increased energy barrier originating from the higher LUMO energy compared to that of ITIC-4F. However, no negative influence is visible in the photodiode regime (i.e., reverse biased junction) where the OPDs are operated. Upon illumination the current increases linearly with incident light intensity as shown in Figure 3b for a bias voltage of −2 V (corresponding current–voltage characteristics are shown in Figure S9 in the Supporting Information). It can be observed that the device current is limited by the dark current floor, whereas the expected saturation in the high intensity range is not reached for the optical incident powers used in this experiment. Therefore, the linear dynamic range (LDR) can be estimated to be >120 dB for both devices which corresponds to typical values reported in other high-performance OPDs.[46–48] Figure 3c displays the effect of bias voltage on the spectral responsivity of the two devices by normalizing the response spectra of ITIC-4F and IDFBR devices at various bias voltages to the corresponding spectrum obtained at −8 V bias. The absolute spectral responsivity curves are depicted in Figure S9 in the Supporting Information. OPDs using PIF:ITIC-4F exhibit an overall higher spectral responsivity starting from 72 mA cm^{-2} at 0 V to 229 mA cm^{-2} at −8 V. These values correspond to external quantum efficiencies (EQE) of 12% and 38%, respectively (see Figure S9 in the Supporting Information). IDFBR devices show a much stronger

effect of the bias voltage on the responsivity, leading to a 12-fold increase from 6 to 73 mA cm^{-2}, equivalent to 1.3% and 17% EQE. This suggests a strongly enhanced charge extraction upon applying a reverse voltage. Since the transmission rate of the signals depends on the dynamic performance of the devices, we also analyze the device characteristics as a function of frequency. In general, for photodetectors, the spectral responsivity declines for high frequencies due to limitations in the charge-carrier transit times and the device RC characteristics.[49] The frequency where the output power reaches 50% of the DC response is termed the −3dB bandwidth or the cutoff frequency. As seen from Figure 3d, the devices show cutoff frequencies of 1.5 and 3.5 MHz under a bias voltage of −2 V for the PIF:ITIC-4F and PIF:IDFBR OPDs, respectively. Furthermore, switching times of 2.5 and 1 μs are measured to switch from 10% to 90% of the amplitude. These values are among the highest values reported for solution processed OPDs particularly in the case of color-selective devices as seen in Table S1 (Supporting Information). This case can be attributed to the favorable morphology and transport properties of the BHJ and a device design that balances transit and RC limitations.[14]

The device performance at lower frequencies, however, is limited by the electrical noise contributions. Typically, three sources of noise are distinguished: i) 1/f noise, ii) thermal noise and iii) shot noise.[14,50–52] While 1/f noise is frequency dependent and is mostly dominant for low frequencies, thermal and shot noise are frequency independent (i.e., white) and scale with the device shunt resistance and dark current, respectively.
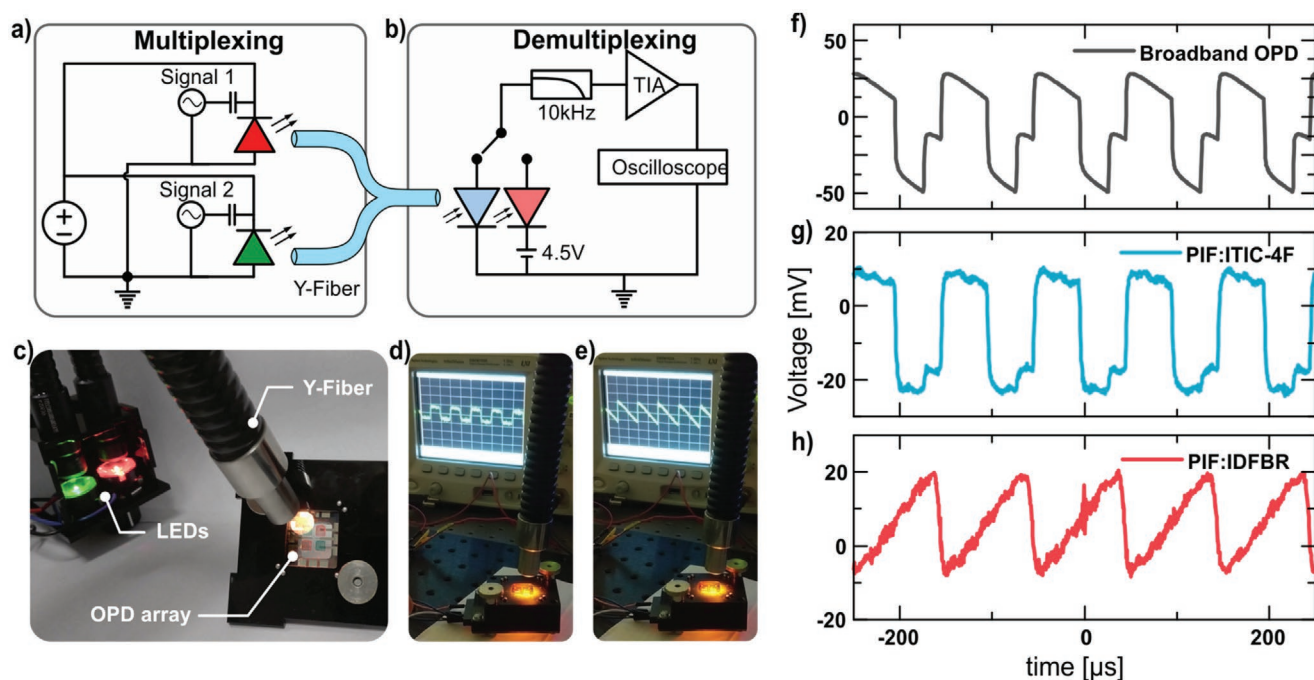
Figure 4. a) Circuit schematic of the multiplexing and b) demultiplexing stage of the VLC system. A red and a green LED are utilized to transmit two independent signals at the same time through an optical fiber. The color-selective OPDs enable a demultiplexing of the combined signal. c) A photograph of the system with the two LEDs, the optical Y-Fiber as well as the printed dual color OPD array. d,e) Photographs of the oscilloscope show the detected signal when either the PIF:ITIC-4F (d) or the PIF:IDFBR (e) device is selected. f–h) Recorded oscilloscope signal under illumination with the intermixed signal of a conventional broadband OPD (f), the PIF:ITIC-4F (g), and the PIF:IDFBR device (h). The color-selective OPDs can successfully demultiplex the signals showing the square and triangular waveforms used to drive the LEDs.

The measured noise spectral density (S_{noise}) of both OPDs at a reverse bias of −2 V is depicted in Figure 3e. Both devices show an almost identical noise curve with negligible difference compared to the 0 V measurement (Figure S10, Supporting Information). Furthermore, the same white noise level of 1.4×10^{-13} A Hz$^{-1/2}$ was found for both devices by fitting the noise measurements with a model assuming a combination of a $1/f$ and a constant contribution.[19] The overlapping S_{noise} suggests that the actual device noise is in the range or below our measurement resolution.

In order to compare the performance between different photodetectors, the specific detectivity D^* is utilized, which is calculated from the spectral responsivity, the electrical noise as well as device area and electronic bandwidth of the measurement set up.[50] Figure 3f displays D^* over a large range of frequencies for both devices. The plateau of the fitting function in Figure 3e was used to extrapolate the noise contribution at higher frequencies. The slope of D^* at lower frequencies stems from the dominant $1/f$ noise contribution. At frequencies >10 Hz, S_{noise} approaches the white noise regime which translates to a constant D^* of 6.9×10^{10} and 1.1×10^{10} Jones for the PIF:ITIC-4F and PIF:IDFBR based devices, respectively. Notably, since the true device noise might be below the measurement resolution, these values serve as a lower limit for D^*. At higher frequencies, the OPDs approach the detection speed limit caused by the reduction of the responsivity, and consequently observe a decay in D^*. The total dynamic performance is therefore limited by noise in the lower frequency regime and by the cutoff frequency in the higher frequency regime.

We designed a VLC system to demonstrate the technological relevance and applicability of the printed color-selective OPDs. The spectral selectivity of the two devices was exploited to directly detect and demultiplex multiple simultaneously transmitted signals at different wavelengths with no additional optical filters. So far similar systems with organic devices were limited to one channel, indirect detection and/or have only been fabricated with nonscalable techniques.[53–55] We decided to perform the VLC transmission at 10 kHz, as this frequency falls into the constant D^* regime. The electronic circuit consists of a multiplexing stage and a demultiplexing stage schematically shown in **Figure 4**a,b. In the multiplexing stage, two LEDs emitting at 530 ± 15 and 627 ± 10 nm were separately driven by two different AC signals. These signals were generated by a waveform generator, a smartphone or a PC, for the various demonstrations where periodic or audio signals were used as the transmitted signal. After coupling both signals into an optical y-fiber, the overlaid signals were demultiplexed by the selective detection of printed PIF:ITIC-4F and PIF:IDFBR OPDs operated at short circuit and at −4.5 V, respectively. Setting the devices at different operating points allows signal differentiation at the wavelength of the green LED to be enhanced. The generated photocurrent was amplified and read by an oscilloscope, or directly connected to loudspeakers as shown in Video S1 in the Supporting Information. To reduce noise in the system, an additional 10 kHz low-pass filter was inserted after the light detection stage. Figure 4c shows a photograph of the VLC system showing the two LED sources in the background, the y-fiber as well as the printed dual color OPD array which

is simultaneously illuminated by both intermixed signals. A square and triangular signal with a frequency of 10 kHz were used to drive the LEDs. Figure 4d,e displays a photograph of the oscilloscope display when one of the color-selective OPDs is selected to detect the intermixed signal. A video of this demonstration is provided in Video S1 in the Supporting Information. Figure 4f–h depicts the output electronic signals of a reference broadband OPD and the two color-selective OPDs, respectively. The signals could be clearly detected and demultiplexed by the color-selective OPDs, while it cannot be separated by the high-performance broadband OPD printed as previously reported by our group.[19] Stacking of the OPDs or signal postprocessing using the complementary response could further improve the selectivity in future applications. We also demonstrate a more practical (and entertaining) application of VLC by replacing the triangular and square inputs with two different audio signals connected via a 3.5 mm audio connector to the LED driving circuits. The oscilloscope on the readout side was replaced by commercial loudspeakers. Both audio signals were transmitted simultaneously through the y-fiber and could be selected freely by simply switching between the two OPDs on the dual color array (Video S2 in the Supporting Information). By using the Shannon-Hartley theorem and assuming a signal-to-noise ratio of 1, the theoretical upper boundary for the data rate can be estimated from the cutoff-frequency to be as high as 3.5 Mbit s^{-1}.[56] Data rates in this range would allow optical transmission of high-definition video content.

In summary, we have demonstrated a novel BHJ approach for the inkjet printing fabrication of high-performance color-selective OPDs and its applicability to VLC. The presented BHJ systems comprised of the optically transparent polymer donor PIF and the NFAs IDFBR and ITIC-4F were analyzed from an energetic, as well as morphological perspective. Both analyses suggest the occurrence of efficient charge generation and separation of excitons formed in the NFA domains which reflects in the high wavelength-selectivity and performance of the presented devices. The approach effectively decouples the viscoelastic and optical properties of the BHJ system. Thus, it opens an unprecedented opportunity to simplify the printing process development of filterless and wavelength-selective OPDs. Finally, we present the first demonstration of a multi-channel VLC system based on a dual-color inkjet-printed OPD array capable of directly demultiplexing various optical signals without the need for additional optical filters. The simplicity of our approach, simultaneously addressing functionality and fabrication, offers a general method for facile integration of wavelength-selective optical sensing elements in future printed electronic applications. Particularly, in those requiring a large degree of personalization, high fabrication throughput and cost-effectiveness such as wearable devices, mobile sensor nodes or healthcare monitoring systems.

Experimental Section

Active Layer Preparation: The materials were separately dissolved in chlorobenzene at a concentration of 20 g L^{-1} (10 g L^{-1} for ATEM samples) and stirred for at least 12 h in a nitrogen filled glovebox. Blends were prepared prior to deposition. For UV–vis and TA measurements,

the materials were spin cast on glass substrates which were cleaned with acetone and isopropanol in an ultrasonic bath. ATEM samples of 30 nm thickness were deposited on a PSS layer to enable the transfer of the layer on holey carbon grids (QUANTIFOIL) grids via a floating process in a demineralized water bath. For printing process evaluation layers were inkjet printed with a Pixdro LP50 (MeyerBurger) using 10 pL 16 nozzle Fujifilm Dimatix cartridges. The cartridge temperature was set to 27 °C. The waveform and ink composition were developed for a pristine PIF solution and kept at the same parameters for the blend solutions. Ink viscosities were measured with a microfluidics rheometer (Rheosense m-vroc).

Layer Characterization: Layers were evaluated optically with a Nikon Eclipse 80i microscope and a UV–vis setup (Light source: AvaLigth-DH-S-BAL, spectrometer: AvaSpec ULS3648). Layer thicknesses and the topography of printed layers were measured with a profilometer (Veeco Dektak 150).

TA measurements were performed under 380, 500, and 650 nm pulsed excitation generated from the fundamental pulses of an amplified Ti:sapphire laser system (35 fs, 800 nm, 1 kHz, 6 mJ, Astrella Coherent). The broadband white light probe pulses were generated by focusing the fundamental beam on a sapphire plate, then split into a reference and a signal component. The pump pulses were generated by frequency converting the fundamental beam in an optical parametric amplifier (OPA, Opera Solo, Coherent) and they were chopped at half the laser frequency. The probe and pump beams had a diameter of 1 mm and 260 µm, respectively, and their relative polarization was set to the magic angle to exclude polarization. The probe pulses were temporally delayed up to 2 ns relative to the excitation pulses via a micrometer translation stage. The signal probe pulses transmitted through the sample and the reference probe pulses were spectrally dispersed in two home-build prism spectrographs, one for the visible and one for the n-IR, assembled by Entwicklungsbüro Stresing, Berlin, Germany, and detected separately, shot-to-shot, by a pair of charge-coupled devices (CCD detectors, Hamamatsu S07030-0906). The TA spectra were corrected for the chirp of the white light probe. Measurements were performed in a sealed chamber under nitrogen atmosphere and signals are averaged over multiple repetitions.

ATEM electron energy-loss imaging and spectroscopy were performed with a Libra 200 MC (Carl Zeiss Microscopy GmbH, Germany) at 60 kV equipped with an in-column energy filter and a monochromator. EEL spectra were recorded from pure layers PIF, ITIC-4F, and IDFBR with thicknesses of around 30 nm. Spectra were normalized by the integral from 5 to 40 eV. ATEM energy-filtered image stacks were acquired from a PIF:ITIC-4F and a PIF:IDFBR layer in the range from 5 to 40 eV at an energy resolution of 1 eV. The total dose for each series was approximately 10^7 electrons nm^{-2}. Details on the data analysis can be found in the Supporting Information.

Device Preparation: OPDs were prepared on prestructured ITO glass substrates which were cleaned with acetone and isopropanol in an ultrasonic bath. A nanoparticle based ZnO ink (N10 Avantama) was used to print the 40 nm thick hole blocking layer on the ITO electrodes. After a postannealing step at 120 °C for 5 min, active blends were printed on top of the ZnO layer with a thickness of 200 nm. The printing pattern was designed to result in a 2 × 2 array of two OPDs with complementary responsivity ranges. Devices were finalized by postprocessing at 140 °C for 10 min in nitrogen atmosphere and thermal evaporation of a molybdenum oxide/silver bilayer (30 nm/100 nm).

Device Characterization: Current voltage measurements in the dark and under illumination with a 500 mW Laser (520 nm; PGL FS-VH) were carried out using a Keithley 2636A source measure unit (SMU). The same SMU was used to apply bias voltages for measurements of the spectral responsivity. A 450 W Osram XBO Xenon discharge lamp served as a broad light source, which was spectrally filtered with a monochromator (Acton SP-2150i). A chopper wheel modulated the light to allow for a measurement with a Stanford Research 830 lock-in amplifier. The current signal was additionally amplified with a Femto DHPCA-100 amplifier.

Noise measurements were carried out in a shielded box using an isolated voltage source (SIM 928) and the SMU to record the amplified current over time (amplifier: Femto DLPCA-200). The temporal signal is afterward Fourier transformed to give the noise spectral density. Details on this method can be found in ref. [19].

The detection speed was evaluated by recording the transient current with an oscilloscope (Agilent DSO 6102A) upon illumination with a square light signal of varying frequency. An Oxxius LBX520 diode laser was used as a light source and modulated by an Agilent 33522A function generator.

VLC System: Two LEDs (Luxeon Rebel LXML green and red) were driven by a PeakTech 6035D current source and simultaneously modulated by a signal of choice. The light signals were coupled into an optical y-fiber and guided to the color-selective OPDs. By manually switching between the OPDs, one of the transmitted signals could be selected. Periodic signals were recorded by the oscilloscope. For the audio signals, the amplified signals were directly connected to a commercial Harman-Kardon 695 sound system.

Supporting Information

Acknowledgements

Conflict of Interest

The authors declare no conflict of interest.

Keywords

[1] B. Nabet, *Photodetectors: Materials, Devices and Applications*, Woodhead Publishing, Cambridge, UK **2016**, pp. 1–525.

[2] K. Chee, *Photodetectors*, IntechOpen, London, UK **2018**.

[3] H. Chun, A. Gomez, C. Quintana, W. Zhang, G. Faulkner, D. O'Brien, *Sci. Rep.* **2019**, *9*, 4952.

[4] J. Lian, Z. Vatansever, M. Noshad, M. Brandt-Pearce, *J. Phys. Photonics* **2019**, *1*, 12001.

[5] R. D. Jansen-van Vuuren, A. Armin, A. K. Pandey, P. L. Burn, P. Meredith, *Adv. Mater.* **2016**, *28*, 4766.

[6] S. Yoon, M. Sim, D. S. Chung, *J. Mater. Chem. C* **2018**, *6*, 13084.

[7] G. Simone, D. Di Carlo Rasi, X. de Vries, G. H. L. Heintges, S. C. J. Meskers, R. A. J. Janssen, G. H. Gelinck, *Adv. Mater.* **2018**, *30*, 1804678.

[8] X. Liu, Y. Lin, Y. Liao, J. Wu, Y. Zheng, *J. Mater. Chem. C* **2018**, *6*, 3499.

[9] F. P. García de Arquer, A. Armin, P. Meredith, E. H. Sargent, *Nat. Rev. Mater.* **2017**, *2*, 16100.

[10] J. Kirkpatrick, C. B. Nielsen, W. Zhang, H. Bronstein, R. S. Ashraf, M. Heeney, I. McCulloch, *Adv. Energy Mater.* **2012**, *2*, 260.

[11] Y. Cui, Y. Wang, J. Bergqvist, H. Yao, Y. Xu, B. Gao, C. Yang, S. Zhang, O. Inganäs, F. Gao, J. Hou, *Nat. Energy* **2019**, *4*, 768.

[12] K.-J. J. Baeg, M. Binda, D. Natali, M. Caironi, Y.-Y. Y. Noh, *Adv. Mater.* **2013**, *25*, 4267.

[13] R. Eckstein, N. Strobel, T. Rödlmeier, K. Glaser, U. Lemmer, G. Hernandez-Sosa, *Adv. Opt. Mater.* **2018**, *6*, 1701108.

[14] N. Strobel, M. Seiberlich, R. Eckstein, U. Lemmer, G. Hernandez Sosa, *Flexible Printed Electron.* **2019**, *4*, 43001.

[15] H. Akkerman, B. Peeters, A. van Breemen, S. Shanmugam, D. Tordera, J.-L. van der Steen, A. J. Kronemeijer, P. Malinowski, F. De Roose, D. Cheyns, J. Genoe, W. Dehaene, P. Heremans, G. Gelinck, *SID Int. Symp. Dig. Tech. Pap.* **2018**, *49*, 494.

[16] R. Eckstein, T. Rödlmeier, T. Glaser, S. Valouch, R. Mauer, U. Lemmer, G. Hernandez-Sosa, *Adv. Electron. Mater.* **2015**, *1*, 1500101.

[17] A. Grimoldi, L. Colella, L. La Monaca, G. Azzellino, M. Caironi, C. Bertarelli, D. Natali, M. Sampietro, *Org. Electron.* **2016**, *36*, 29.

[18] A. Pierre, I. Deckman, P. B. Lechêne, A. C. Arias, *Adv. Mater.* **2015**, *27*, 6411.

[19] N. Strobel, M. Seiberlich, T. Rödlmeier, U. Lemmer, G. Hernandez-Sosa, *ACS Appl. Mater. Interfaces* **2018**, *10*, 42733.

[20] M. Cesarini, B. Brigante, M. Caironi, D. Natali, *ACS Appl. Mater. Interfaces* **2018**, *10*, 32380.

[21] M. Biele, C. Montenegro Benavides, J. Hürdler, S. F. Tedde, C. J. Brabec, O. Schmidt, *Adv. Mater. Technol.* **2019**, *4*, 1800158.

[22] I. Deckman, P. B. Lechêne, A. Pierre, A. C. Arias, *Org. Electron.* **2018**, *56*, 139.

[23] A. Armin, R. D. Jansen-Van Vuuren, N. Kopidakis, P. L. Burn, P. Meredith, *Nat. Commun.* **2015**, *6*, 6343.

[24] J. Kim, S. Yoon, K. M. Sim, D. S. Chung, *J. Mater. Chem. C* **2019**, *7*, 4770.

[25] M. B. Johnston, *Nat. Photonics* **2015**, *9*, 634.

[26] A. Yazmaciyan, P. Meredith, A. Armin, *Adv. Opt. Mater.* **2019**, 1801543.

[27] Z. Tang, Z. Ma, A. Sánchez-Díaz, S. Ullbrich, Y. Liu, B. Siegmund, A. Mischok, K. Leo, M. Campoy-Quiles, W. Li, K. Vandewal, *Adv. Mater.* **2017**, *29*, 1702184.

[28] B. Siegmund, A. Mischok, J. Benduhn, O. Zeika, S. Ullbrich, F. Nehm, M. Böhm, D. Spoltore, H. Fröb, C. Körner, K. Leo, K. Vandewal, *Nat. Commun.* **2017**, *8*, 15421.

[29] P. Westacott, J. R. Tumbleston, S. Shoaee, S. Fearn, J. H. Bannock, J. B. Gilchrist, S. Heutz, J. Demello, M. Heeney, H. Ade, J. Durrant, D. S. McPhail, N. Stingelin, *Energy Environ. Sci.* **2013**, *6*, 2756.

[30] W. Zhang, J. Smith, R. Hamilton, M. Heeney, J. Kirkpatrick, K. Song, S. E. Watkins, T. Anthopoulos, I. Mcculloch, *J. Am. Chem. Soc.* **2009**, *131*, 10814.

[31] W. Zhao, S. Li, H. Yao, S. Zhang, Y. Zhang, B. Yang, J. Hou, *J. Am. Chem. Soc.* **2017**, *139*, 7148.

[32] D. Baran, R. S. Ashraf, D. A. Hanifi, M. Abdelsamie, N. Gasparini, J. A. Röhr, S. Holliday, A. Wadsworth, S. Lockett, M. Neophytou, C. J. M. Emmott, J. Nelson, C. J. Brabec, A. Amassian, A. Salleo, T. Kirchartz, J. R. Durrant, I. McCulloch, *Nat. Mater.* **2017**, *16*, 363.

[33] M. Pfannmöller, H. Flügge, G. Benner, I. Wacker, C. Sommer, M. Hanselmann, S. Schmale, H. Schmidt, F. A. Hamprecht, T. Rabe, W. Kowalsky, R. R. Schröder, *Nano Lett.* **2011**, *11*, 3099.

[34] B. A. Collins, J. R. Tumbleston, H. Ade, *J. Phys. Chem. Lett.* **2011**, *2*, 3135.

[35] W. Köntges, P. Perkhun, R. R. Schröder, E. Barulina, O. Margeat, C. Videlot-Ackermann, J. Ackermann, M. Pfannmöller, in *Proc. NanoGe Fall Meet.*, Fundacio Scito, Valencia, Spain **2019**, https://www.nanoge.org/proceedings/NFM19/5d1206d8c4eeba5c9e2d1827.

[36] M. Pfannmöller, W. Kowalsky, R. R. Schröder, *Energy Environ. Sci.* **2013**, *6*, 2871.

[37] J. C. Brauer, Y. H. Lee, M. K. Nazeeruddin, N. Banerji, *J. Phys. Chem. Lett.* **2015**, *6*, 3675.

[38] Y. Zhong, M. T. Trinh, R. Chen, G. E. Purdum, P. P. Khlyabich, M. Sezen, S. Oh, H. Zhu, B. Fowler, B. Zhang, W. Wang, C. Y. Nam, M. Y. Sfeir, C. T. Black, M. L. Steigerwald, Y. L. Loo, F. Ng, X. Y. Zhu, C. Nuckolls, *Nat. Commun.* **2015**, *6*, 8242.

[39] Y. Tamai, Y. Fan, V. O. Kim, K. Ziabrev, A. Rao, S. Barlow, S. R. Marder, R. H. Friend, S. M. Menke, *ACS Nano* **2017**, *11*, 12473.

[40] N. D. Eastham, J. L. Logsdon, E. F. Manley, T. J. Aldrich, M. J. Leonardi, G. Wang, N. E. Powers-Riggs, R. M. Young, L. X. Chen, M. R. Wasielewski, F. S. Melkonyan, R. P. H. Chang, T. J. Marks, *Adv. Mater.* **2018**, *30*, 1704263.

[41] Y. Liu, L. Zuo, X. Shi, A. K.-Y. Jen, D. S. Ginger, *ACS Energy Lett.* **2018**, *3*, 2396.

[42] Z. Zheng, O. M. Awartani, B. Gautam, D. Liu, Y. Qin, W. Li, A. Bataller, K. Gundogdu, H. Ade, J. Hou, *Adv. Mater.* **2017**, *29*, 1604241.

[43] S. Holliday, R. S. Ashraf, A. Wadsworth, D. Baran, S. A. Yousaf, C. B. Nielsen, C.-H. Tan, S. D. Dimitrov, Z. Shang, N. Gasparini, M. Alamoudi, F. Laquai, C. J. Brabec, A. Salleo, J. R. Durrant, I. McCulloch, *Nat. Commun.* **2016**, *7*, 11585.

[44] D. Qian, Z. Zheng, H. Yao, W. Tress, T. R. Hopper, S. Chen, S. Li, J. Liu, S. Chen, J. Zhang, X. K. Liu, B. Gao, L. Ouyang, Y. Jin, G. Pozina, I. A. Buyanova, W. M. Chen, O. Inganäs, V. Coropceanu, J. L. Bredas, H. Yan, J. Hou, F. Zhang, A. A. Bakulin, F. Gao, *Nat. Mater.* **2018**, *17*, 703.

[45] A. C. Jakowetz, M. L. Böhm, J. Zhang, A. Sadhanala, S. Huettner, A. A. Bakulin, A. Rao, R. H. Friend, *J. Am. Chem. Soc.* **2016**, *138*, 11672.

[46] M. Kielar, O. Dhez, G. Pecastaings, A. Curutchet, L. Hirsch, *Sci. Rep.* **2016**, *6*, 39201.

[47] J. Huang, J. Lee, J. Vollbrecht, V. V. Brus, A. L. Dixon, D. X. Cao, Z. Zhu, Z. Du, H. Wang, K. Cho, G. C. Bazan, T. Nguyen, *Adv. Mater.* **2019**, *32*, 1906027.

[48] C. Montenegro Benavides, S. Rechberger, E. Spiecker, M. Berlinghof, T. Unruh, M. Biele, O. Schmidt, C. J. Brabec, S. F. Tedde, *Org. Electron.* **2018**, *54*, 21.

[49] S. Valouch, M. Nintz, S. W. Kettlitz, N. S. Christ, U. Lemmer, *IEEE Photonics Technol. Lett.* **2012**, *24*, 596.

[50] Y. Fang, A. Armin, P. Meredith, J. Huang, *Nat. Photonics* **2019**, *13*, 1.

[51] S. Xiong, L. Li, F. Qin, L. Mao, B. Luo, Y. Jiang, Z. Li, J. Huang, Y. Zhou, *ACS Appl. Mater. Interfaces* **2017**, *9*, 9176.

[52] G. Simone, M. J. Dyson, S. C. J. Meskers, R. A. J. Janssen, G. H. Gelinck, *Adv. Funct. Mater.*, https://doi.org/10.1002/adfm.201904205.

[53] S. Lee, H. Kim, Y. Kim, *ACS Omega* **2019**, *4*, 3611.

[54] H. Guo, Y. Wang, R. Wang, S. Liu, K. Huang, T. Michinobu, G. Dong, *ACS Appl. Mater. Interfaces* **2019**, *11*, 16758.

[55] W. Li, S. Li, L. Duan, H. Chen, L. Wang, G. Dong, Z. Xu, *Org. Electron.* **2016**, *37*, 346.

[56] C. E. Shannon, *Proc. IRE* **1949**, *37*, 10.